

ASASSN-16dt and ASASSN-16hg: Promising Candidates for a Period Bouncer

Mariko KIMURA^{1,*}, Keisuke ISOGAI¹, Taichi KATO¹, Kenta TAGUCHI², Yasuyuki WAKAMATSU¹, Franz-Josef HAMBSCH^{3,4,5}, Berto MONARD^{6,7}, Gordon MYERS⁸, Shawn DVORAK⁹, Peter STARR¹⁰, Stephen M. BRINCAT¹¹, Enrique de MIGUEL^{12,13}, Joseph ULOWETZ¹⁴, Hiroshi ITOH¹⁵, Geoff STONE¹⁶, Daisaku NOGAMI¹
mkimura@kustastro.kyoto-u.ac.jp

¹*Department of Astronomy, Graduate School of Science, Kyoto University, Oiwakecho, Kitashirakawa, Sakyo-ku, Kyoto 606-8502*

²*Faculty of Science, Kyoto University, Oiwakecho, Kitashirakawa, Sakyo-ku, Kyoto 606-8502*

³*Groupe Européen d'Observations Stellaires (GEOS), 23 Parc de Levesville, 28300 Bailleul l'Evêque, France*

⁴*Bundesdeutsche Arbeitsgemeinschaft für Veränderliche Sterne (BAV), Munsterdamm 90, 12169 Berlin, Germany*

⁵*Vereniging Voor Sterrenkunde (VVS), Oude Bleken 12, 2400 Mol, Belgium*

⁶*Bronberg Observatory, Center for Backyard Astrophysics Pretoria, PO Box 11426, Tiegterpoort 0056, South Africa*

⁷*Kleinkaroo Observatory, Center for Backyard Astrophysics Kleinkaroo, Sint Helena 1B, PO Box 281, Calitzdorp 6660, South Africa*

⁸*Center for Backyard Astrophysics San Mateo, 5 inverness Way, Hillsborough, CA 94010, USA*

⁹*Rolling Hills Observatory, 1643 Nightfall Drive, Clermont, Florida 34711, USA*

¹⁰*Warrumbungle Observatory, Tenby, 841 Timor Rd, Coonabarabran NSW 2357, Australia*

¹¹*Flarestar Observatory, San Gwann SGN 3160, Malta*

¹²*Departamento de Ciencias Integradas, Facultad de Ciencias Experimentales, Universidad de Huelva, 21071 Huelva, Spain*

¹³*Center for Backyard Astrophysics, Observatorio del CIECEM, Parque Dunar, Matalascañas, 21760 Almonte, Huelva, Spain*

¹⁴*Center for Backyard Astrophysics Illinois, Northbrook Meadow Observatory, 855 Fair Ln, Northbrook, Illinois 60062, USA*

¹⁵*Variable Star Observers League in Japan (VSOLJ), 1001-105 Nishiterakata, Hachioji, Tokyo 192-0153*

¹⁶*Sierra Remote Observatories, 44325 Alder Heights Road, Auberry, CA USA*

(Received ; accepted)

Abstract

We present optical photometry of superoutbursts in 2016 of two WZ Sge-type dwarf novae (DNe), ASASSN-16dt and ASASSN-16hg. Their light curves showed a dip in brightness between the first plateau stage with no ordinary superhumps (or early superhumps) and the second plateau stage with ordinary superhumps. We find that the dip is produced by slow evolution of the 3:1 resonance tidal instability and that it would be likely observed in low mass-ratio objects. The estimated mass ratio ($q \equiv M_2/M_1$) from the period of developing (stage A) superhumps (0.06420(3) d) was 0.036(2) in ASASSN-16dt. Additionally, its superoutburst has many properties similar to those in other low- q WZ Sge-type DNe: long-lasting stage A superhumps, small superhump amplitudes, long delay of ordinary superhump appearance, and slow decline rate in the plateau stage with superhumps. The very small mass ratio and observational characteristics suggest that this system is one of the best candidates for a period bouncer – a binary accounting for the missing population of post-period minimum cataclysmic variables. Although it is not clearly verified due to the lack of detection of stage A superhumps, ASASSN-16hg might be a possible candidate for a period bouncer on the basis of the morphology of its light curves and the small superhump amplitudes. Many outburst properties of period-bouncer candidates would originate from the small tidal effects by their secondary stars.

Key words: accretion, accretion disks - novae, cataclysmic variables - stars: dwarf novae - stars: individual (ASASSN-16dt, ASASSN-16hg)

1. Introduction

Dwarf novae (DNe) are a subtype of cataclysmic variables (CVs), and are close binary systems composed of a white dwarf (the primary), typically a late-type main sequence star (the secondary), and an accretion disk around the primary. They go through episodic abrupt increases of luminosity which are called “outbursts” (see Warner 1995 for a review).

WZ Sge-type stars are an extreme subclass of DNe, and belong to SU UMa-type DNe. They have small mass ratios, and predominantly show superoutbursts defined as long-duration (more than ~ 2 weeks) and large-amplitude (more than ~ 6 mag) outbursts with superhumps (see Kato 2015 for a review and references therein). The superoutbursts and superhumps are believed to be caused due to the tidal instability, which is triggered when the disk expands beyond the 3:1 resonance radius

(Osaki 1989; Whitehurst 1988; Hirose, Osaki 1990; Lubow 1991a; Lubow 1991b). Kato et al. (2009) proposed that the superhumps are classified into three stages by the variations of periods and amplitudes: stage A superhumps with a longer and constant period and increasing amplitudes, stage B ones with a systematically varying period and decreasing amplitudes, and stage C ones with a shorter and constant period and increasing amplitudes. The most distinguishing properties of WZ Sge-type DNe are double-peaked modulations called “early superhumps” and rebrightenings.¹ Early superhumps are observed at the early stage of the superoutburst, and have a period almost equal to the orbital one (Kato 2002; Ishioka et al. 2002). Rebrightenings are observed just after the main superoutburst (Imada et al. 2006; Kato et al. 2009; Kato et al. 2014b). The early superhumps are considered to be triggered by the tidal instability when the disk expands beyond the 2:1 resonance radius (Osaki, Meyer 2002; Osaki, Meyer 2003).

The evolutionary status of CVs which have low mass ratios, including WZ Sge-type DNe is still unclear (see Knigge et al. (2011) and references therein). One of the unsolved problems is the gap between the theoretically predicted and observational populations of period bouncers. Period bouncers are CVs past the period minimum, and evolve toward longer orbital periods due to the change of mass-radius relation of the secondary star. This change is triggered by that the thermal timescale becomes longer than the mass-loss timescale or that the secondary degenerates to a brown dwarf at the final stage of the CV evolution (Rappaport et al. 1982; Chabrier et al. 2009). Only a few period bouncer candidates have so far been found, although existing theory predicts that period bouncers should constitute most of the CV population (Kolb 1993). For example, Littlefair et al. (2006) and Littlefair et al. (2008) detected that the companion stars in 4 eclipsing CVs having periods close to the period minimum may be brown dwarfs by modeling their eclipsing light curves. It was demonstrated that one of the systems has a very low-mass brown-dwarf companion by spectroscopic observations (Hernández Santisteban et al. 2016). Unda-Sanzana et al. (2008) found a CV which would have a brown-dwarf companion and a very low mass ratio. Aviles et al. (2010) also detected a brown-dwarf binary with a likely small mass ratio.

Recently, several period-bouncer candidates possibly filling the gap between the theories and observations have been discovered among WZ Sge-type DNe via photometric observations (Kato et al. 2013b; Nakata et al. 2014). These objects showed peculiar rebrightenings, and have very small mass ratios and relatively long orbital periods as WZ Sge-type DNe (more than 0.06 d). Their mass ratios were estimated using a new method which requires the stage A superhump periods and orbital periods (Kato, Osaki 2013). As for SSS J122221.7–311523,

one of these candidates, the evidence suggesting a brown-dwarf companion has also been found (Neustroev et al. 2017). Nakata et al. (2014) also discussed that the detected fraction of these candidates can account for the theoretically expected population of period bouncers. In addition, Kimura et al. (2016) reported that one of WZ Sge-type DNe, which showed a peculiar main superoutburst, may have a small mass ratio. The common properties in this kind of objects are as follows: (1) repeating rebrightenings or dips in brightness at the main superoutburst stage, (2) long-lasting stage A superhumps, (3) large decrease of the superhump period at the stage A to B transition in the objects with repeating rebrightenings, (4) small superhump amplitudes ($\lesssim 0.1$ mag), (5) long delay of ordinary superhump appearance, (6) slow fading rates at the plateau stage of superoutburst with ordinary superhumps, and (7) large outburst amplitude at the time of appearance of ordinary superhumps (Table 1; Sec. 7.8 of Kato 2015).

In this paper, we report on our optical photometry of the 2016 superoutbursts of two WZ Sge-type objects, ASASSN-16dt and ASASSN-16hg. Their outbursts were detected on April 1st, 2016 and April 30th, 2016 by the All-Sky Automated Survey for Supernovae (ASAS-SN) (Shappee et al. 2014; Davis et al. 2015), respectively, and these two objects were regarded as bright CV candidates by that survey because of the large outburst amplitudes.² ASASSN-16dt has a quiescent counterpart PSO J122625.408–113302.953 ($g = 20.76(5)$ mag) and its position is (RA:) 12h26m25.41s, (Dec:) $-11^{\circ}33'03''$ (J2000.0) (Flewelling et al. 2016). ASASSN-16hg has a GALEX UV source and the quiescence magnitude in *NUV* band is 22.8(4) mag. The position of this object is (RA:) 22h48m41.03s, (Dec:) $-35^{\circ}04'40''.1$ (J2000.0). After our observational campaigns, these two objects were regarded as WZ Sge-type DNe by the long delay of superhump appearance and/or early superhumps, and the rebrightenings just after the main superoutbursts. We discuss the properties of these two objects, comparing with those of other period-bouncer candidates.

2. Observation and Analysis

Time-resolved CCD photometric observations were performed at 11 sites by the Variable Star Network (VSNET) collaboration team (Table E1). The logs of the observations of ASASSN-16dt and ASASSN-16hg with clear filter are given in Table E2 and E3, respectively. In this study, the data from the American Association of Variable Star Observers (AAVSO) archive³ are also contained. We converted all of the observation times to barycentric Julian date (BJD). We applied zero-point corrections to each observer by adding constants before making the analyses. The magnitude scale of each site was adjusted to that of the Berto Monard system (MLF in Table E2), where USNO-B1.0 0784-0248445 (RA: 12h26m16.102,

¹ Early superhumps are, however, difficult to be detected in high-inclination systems. In addition, some of WZ Sge-type DNe show no rebrightening, but multiple rebrightenings are exclusive to WZ Sge-type stars (Kato 2015).

² <http://www.astronomy.ohio-state.edu/asasn/transients.html>

³ <http://www.aavso.org/data/download/>

Table 1. Properties of candidates for a period bouncer (The candidates are limited to the DNe which have been through outbursts).

Object*	P_{shB} (d) [†]	Amp [‡]	Delay [§]	Decrease [#]	Profile [¶]	Decline ^{**}	References ^{††}
MASTER J2112	0.060221(9)	0.10	~12	2.2%	B	0.127(1)	1
MASTER J2037	0.061307(9)	0.11	–	2.2%	B, slow	0.052(1)	1
SSS J1222	0.07649(1)	0.12	≥9	0.93%	E, slow	0.020(1)	2, 3
OT J1842	0.07234	0.08	~30	–	E, slow	0.045(1)	2, 4
OT J1735	–	–	–	–	slow	0.038(1)	5
OT J0754	0.070758(6)	0.05	–	2.0%	slow	0.0189(3)	6
OT J2304	0.06635(1)	0.13	–	1.3%	slow	0.0340(4)	6
ASASSN-14cv	0.06045(1)	0.07	14	2.0%	B	0.087(1)	7, 8
PNV J1714	0.060084(4)	0.09	11	2.0%	B	0.108(1)	7, 8
OT J0600	0.063310(4)	0.06	–	2.1%	B	0.080(1)	7, 8
PNV J172929	0.06028(2)	0.12	11	1.7%	D	0.094(1)	8
ASASSN-15jd	0.064981(8)	0.09	10	–	e	0.088(2)	9
ASASSN-15gn	0.06364(3)	0.10	11	–	–	0.0635(7)	10
ASASSN-15hn	0.06183(2)	0.10	12	2.2%	–	0.080(3)	10
ASASSN-15kh	0.06048(2)	0.08	≥13	1.7%	–	0.0601(6)	10
ASASSN-16bu	0.06051(7)	0.10	9	0.62%	slow	0.024(1)	10
ASASSN-16js	0.06093(2)	0.23	10	1.2%	–	0.085(1)	11
ASASSN-16dt	0.064610(1)	0.08	~23	0.79%	E, slow	0.0282(6)	This work
ASASSN-16hg	0.062371(14)	0.12	≥6	–	e, B	0.090(2)	This work

*Objects' name; MASTER J2112, MASTER J2037, SSS J1222, OT J1842, OT J1735, OT J0754, OT J2304, PNV J1714, OT J0600 and PNV J172929 represent MASTER OT J211258.65+242145.4, MASTER OT J203749.39+552210.3, SSS J122221.7–311523, OT J184228.1+483742, OT J173516.9+154708, OT J075418.7+381225, OT J230425.8+062546, PNV J17144255–2943481, OT J060009.9+142615 and PNV J17292916+0054043, respectively.

[†]Period of stage B superhumps.

[‡]Mean amplitude of superhumps. Unit of mag.

[§]Delay time of ordinary superhump appearance. Unit of days.

[#]Decrease rate of stage B superhump period in comparison with stage A superhump period.

[¶]Characteristic shapes of light curves. B: multiple rebrightenings (type-B), D: no rebrightening (type-D), E: double superoutbursts (type-E), e: a small dip in the middle of the plateau, slow: extremely slow fading rate less than ~ 0.05 [mag d⁻¹].

^{**}Fading rate of plateau stage. Unit of mag d⁻¹.

^{††}1: Nakata et al. (2013), 2: Kato et al. (2013b), 3: Neustroev et al. (2017), 4: Katysheva et al. (2013), 5: Kato et al. (2014b), 6: Nakata et al. (2014), 7: Nakata et al. in preparation, 8: Kato et al. (2015), 9: Kimura et al. (2016), 10: Kato et al. (2016), 11: Kato et al. (2017)

Dec:-11°35'03"97, $V = 13.6$) was used as the comparison star in the photometry of ASASSN-16dt, and that of the Franz-Josef Hamsch system (HaC in Table E2), where UCAC4 276–217322 (RA: 22h48m45.56s, Dec:-34°58'50"8, $V = 14.4$) was used as the comparison star in the photometry of ASASSN-16hg, respectively. The constancy of each comparison star was checked by nearby stars in the same images. The data reduction and the calibration of the comparison stars were performed by each observer. The magnitude of each comparison star was measured by the AAVSO Photometric All-Sky Survey (APASS: Henden et al. 2016) from the AAVSO Variable Star Database⁴.

We used the phase dispersion minimization (PDM) method (Stellingwerf 1978) for period analyses. The global trends of the light curves were subtracted by locally-weighted polynomial regression (LOWESS:

Cleveland 1979) before the PDM analyses. We computed the 1σ errors of the best estimated periods by these analyses using the methods of Fernie (1989) and Kato et al. (2010).

In estimating the robustness of the PDM result, we used a variety of bootstraps. We made 100 samples, each of which includes randomly the 50% of observations, and performed PDM analyses for the samples. The result of the bootstrap is represented in the form of 90% confidence intervals in the resultant θ statistics.

3. ASASSN-16dt

3.1. Overall Light Curve

We show the overall light curve of the 2016 superoutburst of ASASSN-16dt in figure 1. The superoutburst probably began on BJD 2457479 and the object showed a rapid rise at the very early stage. A first plateau stage continued for at least 15 days during BJD 2457482.1–

⁴ <<http://www.aavso.org/vsp>>

2457497.1. A dip of brightness was observed in the days BJD 2457499 and BJD 2457500. A rapid increase in brightness was observed for the following ~ 2 days, and the second plateau stage continued for about two weeks during BJD 2457504.0–2457516.8. A rapid fading was seen on BJD 2457518. There were no observations during BJD 2457524–2457530. A rebrightening was detected for a few days during BJD 2457531.8–2457534.5.

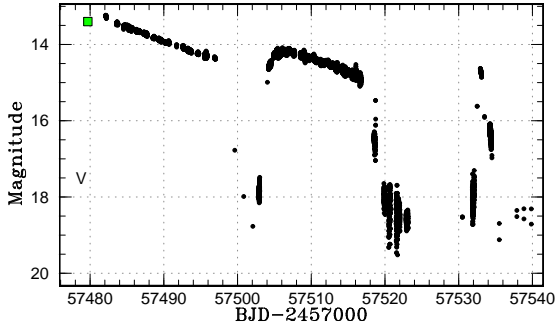


Fig. 1. Overall light curve of the 2016 superoutburst of ASASSN-16dt (BJD 2457478–2457540). The ‘V’-shape and quadrangle represent the upper limit and the detection by ASAS-SN, respectively.

3.2. Early Superhumps

Before the rapid decrease on BJD 2457499, double-waved modulations with a constant period, 0.06420(2) d, were detected. They lasted during BJD 2457482.1–2457493.0. After BJD 2457483, the humps became noisy. We regard them as early superhumps. Figure 2 represents the results of the PDM analysis and the phase-averaged profile of the early superhumps.

3.3. Ordinary Superhumps

During the dip (on BJD 2457502), ordinary superhumps started to develop. The $O-C$ curve of times of superhump maxima, the amplitudes of superhumps, and the light curves during BJD 2457502.8–2457522.1 are shown in the upper panel, the middle panel and the lower panel of figure 3, respectively. We determined the times of maxima and amplitudes of ordinary superhumps in the same way as in Kato et al. (2009). Some points with large errors were removed in calculating the $O-C$ and amplitudes. The resultant times are given in Table E4. We regarded the term of stage A as BJD 2457502.8–2457506.8 ($0 \leq E \leq 58$) from both the $O-C$ curve and the variations of the superhump amplitudes. We determine the term of stage B as being BJD 2457506.8–2457516.8 ($62 \leq E \leq 214$), from the nonlinear behavior on the $O-C$ curve and the decreasing amplitudes of superhumps. No stage C superhumps were found. The superhumps continued after the termination of the main superoutburst. At the post-superoutburst stage during BJD 2457519.9–2457522.0 ($263 \leq E \leq 295$), the superhumps having a longer period than the stage B superhumps were detected.

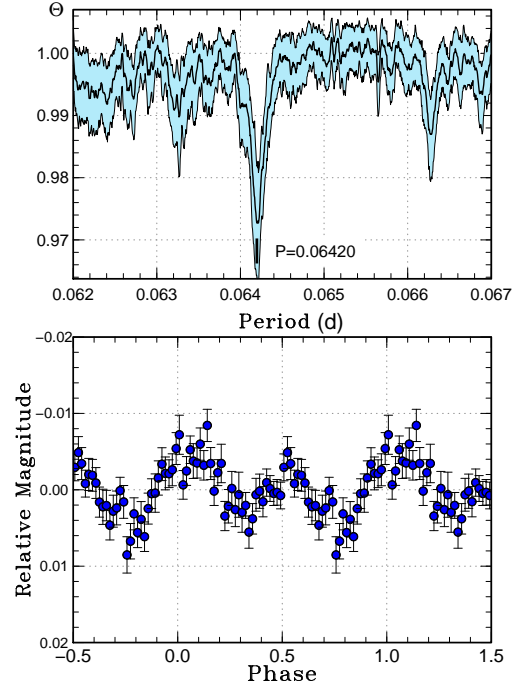


Fig. 2. Early superhumps in the 2016 superoutburst of ASASSN-16dt. The area of gray scale means 1σ errors. Upper: Θ -diagram of our PDM analysis (BJD 2457482.1–2457493.0). Lower: Phase-averaged profile.

Some modulations were seen at the rebrightening; however, we were not able to detect the superhump maxima and periods.

We applied period analyses by the PDM method for stage A and stage B, and obtained periods of $P_{\text{shA}} = 0.06512(1)$ d and $P_{\text{shB}} = 0.064507(5)$ d (see the upper panels of figure 4). Here, the data having low accuracy were excluded from the light curve when we performed our PDM analyses. The derivative of the superhump period during stage B was $P_{\text{dot}}(\equiv \dot{P}_{\text{sh}}/P_{\text{sh}}) = -1.6(0.5) \times 10^{-5} \text{ s}^{-1}$. The mean profiles of superhumps are also shown in the lower panels of figure 4. In addition, the estimated period of the superhumps at the post-superoutburst stage was 0.06493(4) d.

4. ASASSN-16hg

4.1. Overall Light Curve

The overall light curve of the 2016 superoutburst in ASASSN-16hg is shown in figure 5. The first plateau stage continued for more than 6 days before a dip in brightness on BJD 2457590. Soon after the dip, the system became bright again and the second plateau stage began and continued for a week during BJD 2457591.6–2457597.9. We detected two rebrightenings after the main superoutburst.

4.2. Ordinary Superhumps

We have found ordinary superhumps in the second plateau stage and at the beginning of the next decay.

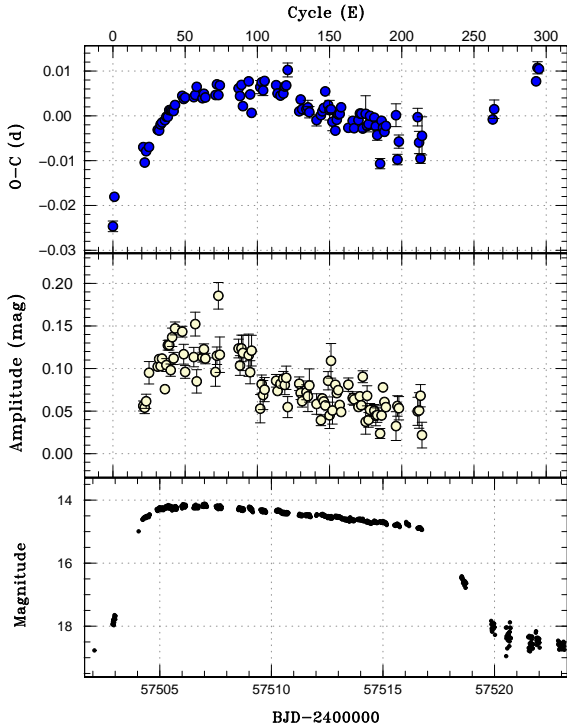


Fig. 3. Upper panel: $O - C$ curve of the times of superhump maxima during BJD 2457502.8–2457522.1 (the second plateau stage of the main superoutburst in ASASSN-16dt). An ephemeris of BJD 2457502.925071+0.0653055 E was used for drawing this figure. Middle panel: amplitudes of superhumps. Lower panel: light curves. The horizontal axis in units of BJD and cycle number is common to these three panels.

The $O - C$ curve of times of superhump maxima, the amplitudes of superhumps and the light curves during the interval are displayed in the upper, middle and lower panels of figure 6, respectively. We determined the times of maxima of ordinary superhumps in the same way as in Sec. 3.3. The resultant times are given in Table E5. We regarded the term during BJD 2457591.6–2457598.8 ($0 \leq E \leq 100$) as stage B judging from the trend of the $O - C$ curve and the decreasing amplitudes. Although there is a possibility that the stage A superhumps appeared between BJD 2457590 (the dip) and BJD 2457591.6 (the initial part of the stage B superhumps), they were not detected due to the low sampling rate of the data and the lack of observations. We were not able to determine whether some modulations before the dip on BJD 2457590 were early superhumps or not since their small amplitudes and the sparse data prevented us from confirming double-waved variations. We note that the different superoutburst stages were not clearly distinguished in the $O - C$ curve.

We applied a period analysis by the PDM method for stage B and obtained the period of $P_{\text{shB}} = 0.06237(1)$ d (see the upper panel of figure 7). The derivative of the superhump period during stage B was $P_{\text{dot}} = 0.6(1.7) \times$

10^{-5} s^{-1} . The mean profile of the stage B superhumps is also shown in the lower panel of figure 7.

5. Discussion

5.1. Mass Ratio Estimation from Stage A Superhumps

We can estimate the mass ratio in ASASSN-16dt using the method proposed by Kato, Osaki (2013), assuming that the early superhump period is identical to the orbital period (Kato 2002; Ishioka et al. 2002). According to Hirose, Osaki (1990), the dynamical precession rate, ω_{dyn} is expressed as follows:

$$\omega_{\text{dyn}}/\omega_{\text{orb}} = Q(q)R(r), \quad (1)$$

where the $Q(q)$ and $R(r)$ are the functions of a mass ratio and a given radius in an accretion disk, respectively (see equations (1) and (2) in Kato, Osaki (2013) for the detailed expressions). Under the assumption that the stage A superhumps are the representation of the dynamical precession at the 3:1 resonance radius, we can derive the value of mass ratio by substituting the 3:1 resonance radius, which is expressed as a function of the mass ratio as $r_{3:1} = 3^{-2/3}(1+q)^{-1/3}$, into equation (1).

The estimated mass ratio with this method is $q = 0.036(2)$ as for ASASSN-16dt. This is shown on the $q - P_{\text{orb}}$ plane in figure 8 with the mass ratios of other period-bouncer candidates and ordinary SU UMA-type DNe derived from Kato et al. (2017). The derived errors originate from the errors of period estimations in Sec. 3. The very small mass ratio suggests ASASSN-16dt is one of the best candidates for a period bouncer. Our result agrees with the empirical relation between rebrightening types and mass ratios, which was suggested in Kato (2015). The q values of candidates for a period bouncer are displayed in Table 2 with those of ordinary WZ Sge-type dwarf novae. Several objects close to the period minimum, which showed repeating rebrightenings, have been shown to be promising period-bouncer candidates because they share the outburst properties with the extremely low- q period-bouncer candidates, and have longer orbital periods than the group of WZ Sge-type DNe whose orbital periods are close to the theoretical period minimum (see also Table 1). The three objects having longer orbital periods than the promising period-bouncer candidates in figure 8 are not regarded as being of this kind, since they do not share the aforementioned properties (see also the 4th paragraph in Sec. 1).

It is shown that some of the objects given in Table 2 would have brown-dwarf secondaries (Littlefair et al. 2008; Savoury et al. 2011; Hernández Santisteban et al. 2016; Neustroev et al. 2017). There may be a possibility that these objects come from zero-age detached white-dwarf and brown-dwarf binaries. Actually, one object which seems to be a pre-CV candidate having a brown-dwarf secondary has recently found (Rappaport et al. 2017). According to Politano (2004), however, $\sim 80\%$ of this kind of detached binaries have small orbital periods less than 0.054 d, and the fraction of them to the total population of zero-age CVs seems to be smaller than

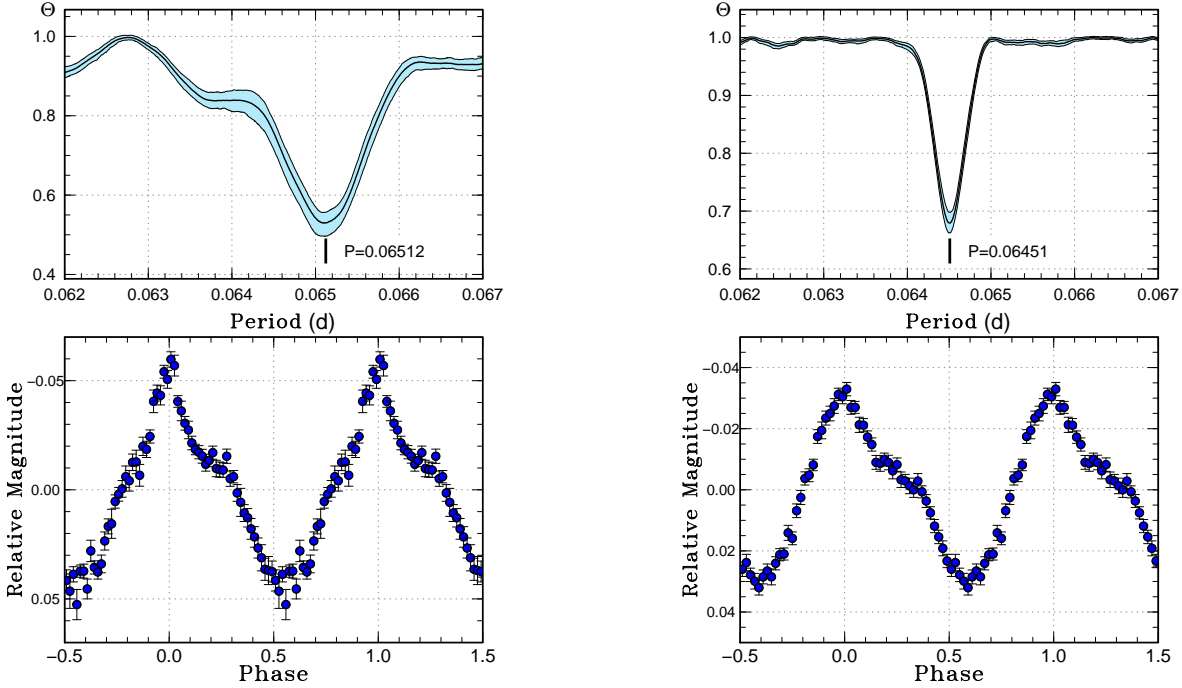


Fig. 4. Stage A and B superhumps in the second plateau stage of the 2016 superoutburst of ASASSN-16dt are represented in the left and right panels, respectively. The area of gray scale means 1σ errors. Upper: Θ -diagrams of our PDM analyses. Lower: Phase-averaged profiles.

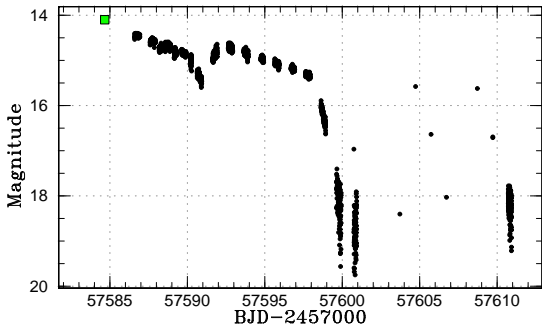


Fig. 5. Overall light curve of the 2016 superoutburst of ASASSN-16hg (BJD 2457584–2457611). The quadrangle represents the detection by ASAS-SN.

a half. Thus some objects in Table 2, which we discuss here, would be formed from the zero-age CVs with main-sequence companions via the mass loss of the companions rather than the zero-age CVs with brown-dwarf companions. This kind of discussion was also stated in Neustroev et al. (2017).

5.2. Dip in Brightness during Main Superoutburst

The dips in brightness during the main superoutbursts were observed in both ASASSN-16dt and ASASSN-16hg. Rebrightenings in WZ Sge-type stars are classified into five types according to the profiles of the light curves: type-A (long duration rebrightening), type-B (multiple rebright-

ening), type-C (single rebrightening), type-D (no rebrightening), and type-E (double superoutbursts consisting of a plateau stage with early superhumps and another plateau stage with ordinary superhumps) (Imada et al. 2006; Kato et al. 2009; Kato et al. 2014b), and ASASSN-16dt belongs to WZ Sge-type objects with double superoutbursts. This object is an analogue of SSS J122221.7–311523 and OT J184228.1+483742 (Kato et al. 2013b; Katysheva et al. 2013; Neustroev et al. 2017). ASASSN-16hg is the second object showing an intermediate light curve between the single plateau stage (in type-A–D rebrightenings) and the double ones (in type-E rebrightening). The details of the classification with the morphology of plateau stages are described in Kimura et al. (2016). In addition, the duration of stage A superhumps is normally long in the candidates (Kato et al. 2013b; Nakata et al. 2014), and also in ASASSN-16dt, the stage A superhumps continued for a long interval, ~ 4 days.

The characteristic morphology of the light curves seems to represent the slow development of the 3:1 resonance which is believed to cause ordinary superhumps since the resonance keeps the disk in the hot state in WZ Sge-type DNe after the disappearance of the 2:1 resonance (Osaki, Meyer 2003). Lubow (1991a) proposed that the growth time of the 3:1 resonance tidal instability is inversely proportional to the square of the mass ratio. The small mass ratio and the morphology of the 2016 superoutburst in ASASSN-16dt are in good agreement with this theory. In addition, the slow growth of the 3:1 resonance is expected to produce the long-lasting stage A superhumps in small- q

Table 2. Mass ratios of candidates for a period bouncer.

Object*	P_{orb} (d) [†]	P_{shA} (d) [‡]	q [§]	References
SDSS J1507	0.046258	–	0.0625(4)	1
SDSS J1433	0.054241	–	0.069(3)	2, 3
SDSS J1501	0.056841	–	0.067(3)	1
SDSS J1035	0.057007	–	0.057(1)	4
ASASSN-16bu	0.0593(1)	0.06089(7)	0.10(1)*	5
PNV J1714	0.059558(3)	0.06130(2)	0.076(1)*	6, 7
PNV J172929	0.05973	0.06133(7)	0.073(2)*	7
MASTER J2112	0.059732(3)	0.06158(5)	0.081(2)*	8
ASASSN-14cv	0.059917(4)	0.06168(2)	0.077(1)*	6, 7
ASASSN-16js	0.060337(5)	0.0617(1)	0.056(5)*	9
MASTER J2037	0.0605(2)	0.0627(1)	0.097(8)*	8
SDSS J1057	0.062792	–	0.055(2)	1
ASASSN-16dt	0.06420(3)	0.06512(1)	0.036(2)*	This work
OT J1842	0.07168(1)	0.07287(8)	0.042(3)*	10
SSS J1222	0.07625(5)	0.07721(1)	0.032(2)*	11, 12

*Objects' name; MASTER J2112, MASTER J2037, SSS J1222, OT J1842, PNV J1714, PNV J172929, SDSS J1057, SDSS J1035, SDSS J1433, SDSS J1501, SDSS 1433, and SDSS 1507 represent MASTER OT J211258.65+242145.4, MASTER OT J203749.39+552210.3, SSS J122221.7–311523, OT J184228.1+483742, PNV J17144255–2943481, PNV J17292916+0054043, SDSS J105754.25+275947.5, SDSS J103533.02+055158.3, SDSS J143317.78+101123.3, SDSS J150137.22+550123.4, SDSS J143317.78+101123.37, and SDSS J150722.30+523039.8, respectively.

[†]Orbital period.

[‡]Period of stage A superhumps.

[§]Mass ratio. The index * represents the mass ratio derived by the method in Kato, Osaki (2013).

^{||}1: McAllister et al. (2017), 2: Littlefair et al. (2008), 3: Hernández Santisteban et al. (2016), 4: Savoury et al. (2011), 5: Kato et al. (2016), 6: Nakata et al. in preparation, 7: Kato et al. (2015), 8: Nakata et al. (2013), 9: Kato et al. (2017), 10: Kato, Osaki (2013), 11: Kato et al. (2013b), 12: Neustroev et al. (2017).

systems. Although the small dip during the main superoutburst in ASASSN-16hg may suggest that this system likely has a small q value, it is unclear whether the ordinary superhumps slowly developed, due to the lack of detection of the initial part of the developing ordinary superhumps (stage A superhumps) (see Sec. 4.2).

5.3. Long Delay of Superhump Appearance

The delays of ordinary superhump appearance are typically long in the candidates for a period bouncer (see Table 1), whilst those in ordinary WZ Sge-type stars are concentrated between 5–10 [d] (Kato 2015). This feature is also clearly confirmed in the 2016 superoutburst of ASASSN-16dt. Figure 9 shows the relation between superhump period and delay time in WZ Sge-type DNe. On the other hand, it is uncertain whether the delay of the superhump appearance was long in ASASSN-16hg since there was no observation between the upper limit by ASAS-SN on BJD 2457573 and the detection by the same survey on BJD 2457584.

In ASASSN-16dt, early superhumps were clearly de-

tected at the early stage of its superoutburst. Osaki, Meyer (2003) proposed that the 2:1 resonance causing early superhumps suppresses the 3:1 resonance. The presence of early superhumps lasting for at least ~ 10 days in ASASSN-16dt support this explanation. As for the objects having very small mass ratios, the disk radius would expand far beyond the 2:1 resonance radius when an outburst is triggered. This is because the stored disk mass naturally become large due to extremely low viscosity in the quiescent disk, while the tidal effect by the secondary is weak in these objects (Osaki, Meyer 2002). Collectively, these effects sustain the 2:1 resonance for a long interval.

5.4. Small Amplitude of Superhumps

Kimura et al. (2016) pointed out that the average superhump amplitudes are small, less than 0.1 mag, in most of the candidates for a period bouncer (Table 1). Our results on ASASSN-16dt and ASASSN-16hg reinforce this observation (see also figures 3 and 6). We compare the variation of superhump amplitudes of the candidates for

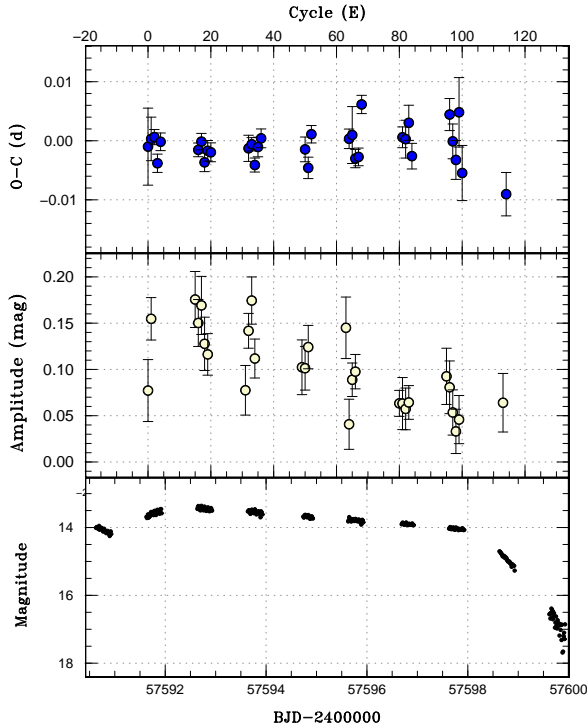


Fig. 6. Upper panel: $O - C$ curve of the times of superhump maxima during BJD 2457591.6–2457598.8 (the second plateau stage of the main superoutburst in ASASSN-16hg). An ephemeris of BJD 57591.6610+0.0623475 E was used for drawing this figure. Middle panel: amplitudes of superhumps. Lower panel: light curves. The horizontal axis in units of BJD and cycle number is common to these three panels.

a period bouncer and those of ordinary SU UMa-type systems having orbital periods ranging between 0.06–0.07 d in figure 10 as in Kimura et al. (2016).⁵ In plotting this figure, we measured the amplitudes using the template fitting method described in Kato et al. (2009) and took the starting point of the cycle count from the start of stage B. Since superhump amplitudes are known to depend on the orbital periods and the inclination angles (Kato et al. 2012), the data of ASASSN-16js are excluded from this figure. This object may have high inclination, which is judged from the large amplitudes of its early superhumps, ~ 0.2 mag (Kato et al. 2017). It is known that the higher the inclination is, the larger the amplitudes of early superhumps are (Kato 2015), and the ~ 0.2 -mag amplitudes of early superhumps are comparable to those of WZ Sge having the inclination of 77 ± 2 deg (Steehgs et al. 2007). The median value of the amplitudes between $-3 < E < 5$ in the period-bouncer candidates is significantly smaller, 0.074 mag, than that in ordinary SU UMa-type DNe, 0.22 mag.

During the 3:1 resonance, the disk becomes elliptical due to the tidal force of the secondary; the orbiting secondary passes the major axis of the disk with the super-

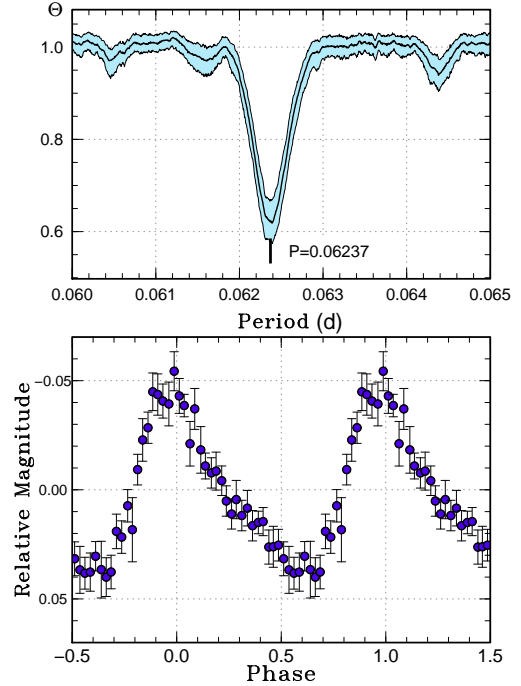


Fig. 7. Stage B superhumps in the second plateau stage of the 2016 superoutburst of ASASSN-16hg are represented. The area of gray scale means 1σ errors. Upper: Θ -diagram of our PDM analysis. Lower: Phase-averaged profile.

hump period when the ordinary superhumps are observed. Some particles in the tail of the eccentric disk are periodically absorbed to the secondary, and the time variations of the released energy by the viscous dissipation in the outer disk corresponds the superhump variations (Hirose, Osaki 1990). It has been proposed that the tidal torques exerted by the secondary significantly affect viscous dissipation in the outer disk (Ichikawa, Osaki 1994). In the small- q objects, the tidal force from the secondary would be less than that in the large- q objects. The disk would be less elliptical and the liberated energy by the tidal dissipation would be small. Thus the reason why period-bouncer candidates show small-amplitude superhumps seems to be related to the weak tidal effect by the secondary in small- q objects.

5.5. Slow Fading Rate of Plateau Stage

The fading rates of the plateau stage with ordinary superhumps in the superoutbursts of period-bouncer candidates are often small (Sec. 7.8 in Kato 2015). In particular, all of the three period-bouncer candidates including ASASSN-16dt, which showed double superoutbursts, had extremely low decline rates (see Table 1). They also have very small mass ratios, and the durations of the superoutbursts are long – more than 40 days (see also Kato et al. 2013b). One period-bouncer candidate with type-B rebrightenings and four other candidates whose rebrightening types have not yet been identified showed slow declines (see also Table 1). The relation between the fading

⁵ We excluded the data with large errors more than 0.03 mag and of eclipsing systems.

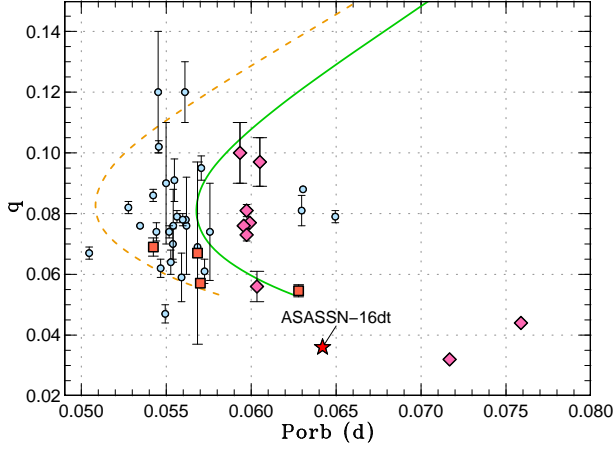


Fig. 8. $q - P_{\text{orb}}$ relation of the candidates for a period bouncer and ordinary WZ Sge-type DNe. The star, diamonds, rectangles and circles represent ASASSN-16dt, other candidates for a period bouncer among the identified WZ Sge-type DNe, the candidates for a period bouncer among eclipsing CVs, and ordinary WZ Sge-type DNe. The dash and solid lines represent an evolutionary track of the standard evolutionary theory and that of the modified evolutionary theory, respectively, which are derived from Knigge et al. (2011).

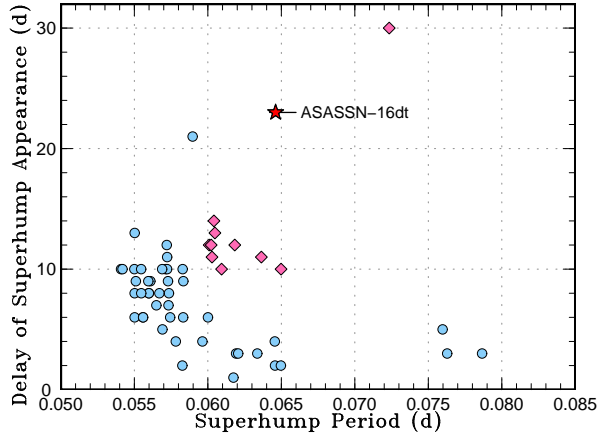


Fig. 9. P_{SH} vs. delay time of ordinary superhump appearance. The circles and diamonds indicate ordinary WZ Sge-type stars derived from Fig. 19 in Kato (2015) and the candidates for a period bouncer. The star represents ASASSN-16dt.

rate and the superhump period is shown in figure 11. The median value of the fading rates in the period-bouncer candidates is 0.06 mag d^{-1} , while that in ordinary WZ Sge-type stars is 0.10 mag d^{-1} .

The decline timescale is proportional to $\alpha^{-0.7}$ (equation (49) in Osaki (1989)). Here α represents the viscous parameter in the hot state, and the combination of ordinary α due to magnetohydrodynamical instability plus the viscosity resulting from the tidal torque (Balbus, Hawley 1991; Ichikawa, Osaki 1994). The slow fading rate in period bouncers would therefore be attributed to the weaker tidal torque in low- q objects.

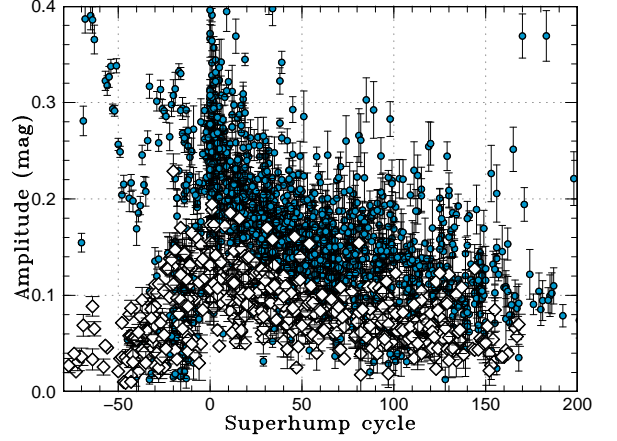


Fig. 10. Variation of superhump amplitudes in the SU UMa-type objects with $0.06 \text{ d} < P_{\text{orb}} \leq 0.07 \text{ d}$. The diamonds and circles represent the candidates for a period bouncer and ordinary SU UMa-type DNe, respectively. The data of the period-bouncer candidates are derived from Nakata et al. (2013); Kato et al. (2013b); Nakata et al. (2014); Kato et al. (2015); Kato et al. (2016); Kimura et al. (2016); Kato et al. (2017), and those of ordinary SU UMa-type DNe are derived from Kato et al. (2009); Kato et al. (2010); Kato et al. (2012); Kato et al. (2013a); Kato et al. (2014b); Kato et al. (2014a); Kato et al. (2015); Kato et al. (2016); Kato et al. (2017).

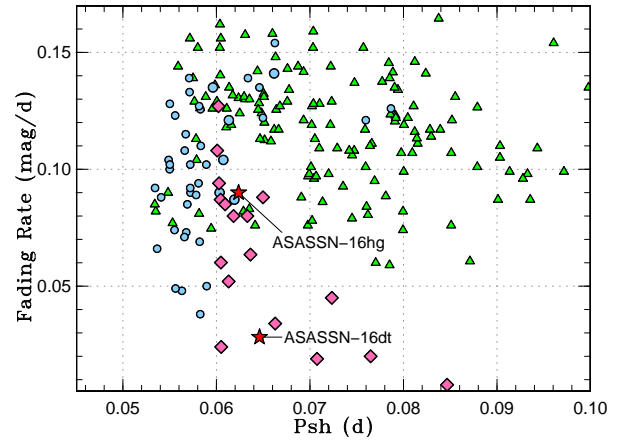


Fig. 11. Fading rate vs. superhump period in stage B. The circles, triangles, and diamonds represent ordinary SU UMa-type DNe, WZ Sge-type DNe, and candidates for the period bouncer, respectively. The stars indicate ASASSN-16dt and ASASSN-16hg. The data of the ordinary SU UMa-type DNe and WZ Sge-type DNe are derived from Kato et al. (2014b).

6. Conclusions

We have reported on our photometric observations of two WZ Sge-type DNe, ASASSN-16dt and ASASSN-16hg, and discussed their similar properties to those of period-bouncer candidates. The important findings are summarized as follows:

- ASASSN-16dt and ASASSN-16hg underwent outbursts with a dip in brightness at their main superoutbursts. This implies that the 3:1 resonance grew slowly in their outbursts, and that these objects have low mass ratios.
- The mass ratio in ASASSN-16dt, estimated from the method of Kato, Osaki (2013) via the stage A superhump period (0.06512(1) d) is 0.036(2), which is much lower than the theoretically expected mass ratio at the period minimum. The relatively long orbital period estimated from the early superhumps and the very low mass ratio are enough to judge that this object is one of the best period-bouncer candidates. This object also showed many features similar to those in other candidates for a period bouncer, featuring long-lasting stage A superhumps and early superhumps, small-amplitude superhumps, and a slow decline rate at the plateau stage.
- Although it is uncertain whether the development of the superhumps in ASASSN-16hg was slow due to no detection of the stage A superhumps, this object might be a possible period-bouncer candidate on the basis of the morphology of the plateau stage which resembles that during the 2015 superoutburst in ASASSN-15jd (Kimura et al. 2016) and its small superhump amplitude.
- Many outburst properties of the period-bouncer candidates would be explained by the small tidal effect by the secondary in small- q systems.

The outburst behavior of candidates for a period bouncer is different from that of ordinary WZ Sge-type stars. It should be confirmed whether this behavior is inherent to the period bouncers, by identifying observational properties of many candidates. Some of the candidates given in Table 2 have not experienced outbursts. It would be interesting to monitor their behavior when they enter outbursts.

Acknowledgements

This work was financially supported by the Grant-in-Aid for JSPS Fellows for young researchers (MK, KI) and by a Grant-in-Aid “Initiative for High-Dimensional Data-Driven Science through Deepening of Sparse Modeling” from the Ministry of Education, Culture, Sports, Science and Technology (MEXT) of Japan (25120007, TK). Also, it was partially supported by the RFBR grant 15-02-06178. We appreciate All-Sky Automated Survey for Supernovae (ASAS-SN) detecting a large amount of DNe. We are thankful to many amateur observers for providing a lot of data used in this research. We are grateful to Ra’ad Mahmoud for correcting the English in this paper. We appreciate an anonymous referee’s giving us helpful comments.

Supporting information

Additional supporting information can be found in the online version of this article: Supplementary tables E1,

E2, E3, E4 and E5.

References

- Aviles, A., et al. 2010, *ApJ*, 711, 389
 Balbus, S. A., & Hawley, J. F. 1991, *ApJ*, 376, 214
 Chabrier, G., Baraffe, I., Leconte, J., Gallardo, J., & Barman, T. 2009, in *15th Cambridge Workshop on Cool Stars, Stellar Systems, and the Sun*, ed. E. Stempels Vol. 1094 of American Institute of Physics Conference Series(. p. 102
 Cleveland, W. S. 1979, *J. Amer. Statist. Assoc.*, 74, 829
 Davis, A. B., Shappee, B. J., Archer Shappee, B., & ASAS-SN 2015, *American Astron. Soc. Meeting Abstracts*, 225, #344.02
 Fernie, J. D. 1989, *PASP*, 101, 225
 Flewelling, H. A., et al. 2016, *arXiv:1612.05243*
 Henden, A. A., Templeton, M., Terrell, D., Smith, T. C., Levine, S., & Welch, D. 2016, *VizieR Online Data Catalog*, 2336
 Hernández Santisteban, J. V., et al. 2016, *Nature*, 533, 366
 Hirose, M., & Osaki, Y. 1990, *PASJ*, 42, 135
 Ichikawa, S., & Osaki, Y. 1994, *PASJ*, 46, 621
 Imada, A., Kubota, K., Kato, T., Nogami, D., Maehara, H., Nakajima, K., Uemura, M., & Ishioka, R. 2006, *PASJ*, 58, L23
 Ishioka, R., et al. 2002, *A&A*, 381, L41
 Kato, T. 2002, *PASJ*, 54, L11
 Kato, T. 2015, *PASJ*, 67, 108
 Kato, T., et al. 2014a, *PASJ*, 66, 90
 Kato, T., et al. 2015, *PASJ*, 67, 105
 Kato, T., et al. 2013a, *PASJ*, 65, 23
 Kato, T., et al. 2014b, *PASJ*, 66, 30
 Kato, T., et al. 2016, *PASJ*, 68, 65
 Kato, T., et al. 2017, *PASJ*, submitted
 Kato, T., et al. 2009, *PASJ*, 61, S395
 Kato, T., et al. 2012, *PASJ*, 64, 21
 Kato, T., et al. 2010, *PASJ*, 62, 1525
 Kato, T., Monard, B., Hamsch, F.-J., Kiyota, S., & Maehara, H. 2013b, *PASJ*, 65, L11
 Kato, T., & Osaki, Y. 2013, *PASJ*, 65, 115
 Katysheva, N., et al. 2013, *Central European Astrophys. Bull.*, 37, 335
 Kimura, M., et al. 2016, *PASJ*, 68, 55
 Knigge, C., Baraffe, I., & Patterson, J. 2011, *ApJ*, 194, 28
 Kolb, U. 1993, *A&A*, 271, 149
 Littlefair, S. P., Dhillon, V. S., Marsh, T. R., Gänsicke, B. T., Southworth, J., Baraffe, I., Watson, C. A., & Copperwheat, C. 2008, *MNRAS*, 388, 1582
 Littlefair, S. P., Dhillon, V. S., Marsh, T. R., Gänsicke, B. T., Southworth, J., & Watson, C. A. 2006, *Science*, 314, 1578
 Lubow, S. H. 1991a, *ApJ*, 381, 259
 Lubow, S. H. 1991b, *ApJ*, 381, 268
 McAllister, M. J., et al. 2017, *MNRAS*, 467, 1024
 Nakata, C., et al. 2014, *PASJ*, 66, 116
 Nakata, C., et al. 2013, *PASJ*, 65, 117
 Neustroev, V. V., et al. 2017, *MNRAS*, 467, 597
 Osaki, Y. 1989, *PASJ*, 41, 1005
 Osaki, Y., & Meyer, F. 2002, *A&A*, 383, 574
 Osaki, Y., & Meyer, F. 2003, *A&A*, 401, 325
 Politano, M. 2004, *ApJ*, 604, 817
 Rappaport, S., Joss, P. C., & Webbink, R. F. 1982, *ApJ*, 254, 616
 Rappaport, S., et al. 2017, *MNRAS*, 471, 948
 Savoury, C. D. J., et al. 2011, *MNRAS*, 415, 2025

- Shappee, B. J., et al. 2014, *ApJ*, 788, 48
Steehhs, D., Howell, S. B., Knigge, C., Gänsicke, B. T., Sion,
E. M., & Welsh, W. F. 2007, *ApJ*, 667, 442
Stellingwerf, R. F. 1978, *ApJ*, 224, 953
Unda-Sanzana, E., et al. 2008, *MNRAS*, 388, 889
Warner, B. 1995, *Cataclysmic Variable Stars* (Cambridge:
Cambridge University Press)
Whitehurst, R. 1988, *MNRAS*, 232, 35

Table E2. List of Instruments.

CODE*	Telescope (& CCD)	Observatory (or Observer)	Site
BSM	25cmSC+Moravian G2-1600	Flarestar Observatory	San Gwann, Malta
deM	35cmSC+QSI-516wsg	Observatorio Astronomico del CIECEM	Huelva, Spain
DKS	25cmACF	Rolling Hills Observatory	USA
HaC	40cmIRDK+FLI-ML16803	Remote Observatory Atacama Desert (ROAD)	San Pedro de Atacama, Chile
Ioh	30cmSC+ST-9XE CCD	Hiroshi Itoh	Tokyo, Japan
MLF	30cmRCX400+ST8-XME	Berto Monard Calitzdorp	South Africa
	35cmRCX400+ST8-XME		
MGW	43.1cmPlanewaveCDK +FLI PL4710 CCD	Gordon Myers	Siding Spring, Australia
KU1	40cmSC+Apogee U6	Kyoto U. Team	Kyoto, Japan
SGE	43cmCDK+STXL-11002	Sierra Remote Observatories	Auberry, CA, USA
SPE	51cmPlanewaveCDK +SBig STL 168303	Warrumbungle & Dubbo Observatory	Australia
UJH	23cmSCT+QSI-583ws	Joseph Ulowetz	USA

*see the annotation in Table E2.

Table E3. Log of observations of the 2016 outburst in ASASSN-16dt.

Start*	End*	Mag [†]	Error [‡]	N^{\S}	Obs
57482.1006	57482.2068	13.199	0.019	84	SPE
57483.5701	57483.7663	13.417	0.020	110	HMB
57484.5278	57484.7410	13.501	0.029	124	HMB
57485.0301	57485.2374	13.491	0.025	116	SPE
57485.2343	57485.4249	-0.018	0.018	549	MLF
57485.5292	57485.7608	13.563	0.021	102	HaC
57486.2857	57486.4086	0.064	0.014	351	MLF
57486.5348	57486.7581	13.623	0.015	106	HMB
57487.2795	57487.3615	0.122	0.012	237	MLF
57487.5282	57487.7552	13.710	0.020	108	HaC
57488.5268	57488.7504	13.793	0.016	106	HaC
57489.2968	57489.4274	0.282	0.014	376	MLF
57489.5268	57489.7497	13.868	0.017	106	HaC
57490.0690	57490.1896	13.874	0.012	94	SPE
57490.5248	57490.7470	13.925	0.019	96	HMB
57491.7255	57491.7457	14.000	0.017	11	HaC
57492.5232	57492.7410	14.046	0.024	95	HaC
57493.2464	57493.4544	0.561	0.018	598	MLF
57493.5602	57493.7401	14.145	0.019	64	HaC
57494.5236	57494.7371	14.204	0.015	137	HaC
57495.5177	57495.7343	14.262	0.032	120	HMB
57495.7321	57495.8591	13.944	0.030	180	SGE
57496.8774	57497.0056	14.283	0.010	162	MGW
57499.5158	57499.7530	16.774	0.352	124	HMB
57500.5370	57500.7504	16.749	0.701	37	HaC
57500.8773	57501.0057	18.604	0.357	156	MGW
57502.8776	57503.0052	17.742	0.129	161	MGW
57504.2149	57504.4214	0.978	0.040	567	MLF
57504.3673	57504.5505	14.572	0.043	207	deM
57504.8605	57505.1721	14.203	0.033	389	MGW
57504.9694	57505.0386	-0.567	0.054	195	KU1
57505.2143	57505.5014	0.639	0.039	823	MLF
57505.2921	57505.4930	14.223	0.046	193	BSM
57505.3857	57505.5202	14.266	0.037	150	deM
57505.5493	57505.7691	14.150	0.040	294	DKS
57505.9719	57506.1719	14.111	0.039	248	MGW
57506.5123	57506.7358	14.223	0.036	130	HMB
57506.8985	57507.1090	14.092	0.034	263	MGW
57507.5114	57507.7671	14.230	0.036	103	HaC
57508.5115	57508.7649	14.285	0.036	121	HMB
57508.9882	57509.1964	14.282	0.168	305	Ioh
57509.5110	57509.7620	14.341	0.033	119	HaC
57510.2135	57510.4897	0.769	0.037	784	MLF
57510.5097	57510.7592	14.418	0.029	136	HaC
57511.0128	57511.0548	-0.425	0.045	118	KU1
57511.2339	57511.4076	0.894	0.030	497	MLF
57511.5121	57511.7565	14.487	0.028	132	HMB
57512.0048	57512.0523	14.489	0.024	30	SPE
57512.2163	57512.4337	0.897	0.027	619	MLF

Table E2. Log of observations of the 2016 outburst in ASASSN-16dt (continued).

Start*	End*	Mag [†]	Error [‡]	N [§]	Obs
57512.5091	57512.7530	14.549	0.029	125	HaC
57512.8567	57513.1718	14.462	0.028	387	MGW
57512.9488	57513.1390	-0.302	0.045	522	KU1
57513.1065	57513.1898	14.591	0.025	64	SPE
57513.2467	57513.4953	1.045	0.032	717	MLF
57513.3047	57513.4691	14.573	0.041	166	BSM
57513.5085	57513.7281	14.622	0.069	103	HaC
57513.6198	57513.7287	14.668	0.021	85	BJA
57513.8567	57514.1253	14.539	0.021	336	MGW
57514.2284	57514.4699	1.118	0.036	587	MLF
57514.5454	57514.7371	14.595	0.031	212	DKS
57514.5834	57514.7549	14.493	0.040	170	UJH
57514.8542	57515.1715	14.629	0.027	397	MGW
57515.5091	57515.7304	14.798	0.062	113	HaC
57515.5454	57515.7477	14.692	0.037	272	DKS
57515.5852	57515.6621	14.534	0.046	35	UJH
57516.0414	57516.1724	14.740	0.087	45	Ioh
57516.5506	57516.7373	14.896	0.026	78	HaC
57516.5512	57516.7362	14.781	0.040	187	DKS
57518.5068	57518.7364	16.521	0.168	117	HaC
57519.8462	57520.0213	18.005	0.134	177	MGW
57520.0184	57520.0209	3.267	0.278	3	KU1
57520.5076	57520.7301	18.318	0.384	100	HaC
57521.5070	57521.7289	18.539	0.376	98	HaC
57521.8505	57522.0214	18.451	0.152	213	MGW
57522.8520	57523.1295	18.614	0.113	186	MGW
57530.5033	57530.5044	18.526	0.002	2	HaC
57531.5030	57531.5041	18.530	0.040	2	HMB
57531.8460	57532.1077	18.158	0.222	172	MGW
57532.5027	57532.5038	15.157	0.003	2	HMB
57532.9298	57533.1074	14.994	0.061	119	MGW
57533.5023	57533.5034	15.437	0.019	2	HaC
57534.5026	57534.5037	16.479	0.046	2	HaC
57535.5020	57535.5031	18.445	0.302	2	HaC
57537.8864	57537.8879	18.433	0.115	2	MGW
57538.8439	57538.8455	18.442	0.188	2	MGW
57539.8442	57539.8457	18.512	0.283	2	MGW
57542.4941	57542.4951	19.788	0.152	2	HaC
57543.4998	57543.5009	19.343	0.325	2	HaC
57544.4993	57544.5004	19.203	0.249	2	HaC
57547.4998	57547.5009	19.261	0.115	2	HaC
57548.5008	57548.5019	19.607	0.607	2	HaC
57551.4941	57551.4952	19.230	0.112	2	HaC

*BJD - 2400000.0.

†Mean magnitude.

‡ 1σ of mean magnitude.

§Number of observations.

||Observer's code: SPE (Peter Starr), HaC (Franz-Josef Hambach), MLF (Berto Monard), SGE (Geoff Stone), MGW (Gordon Myers), deM (Enrique de Miguel), KU1 (Kyoto Univ. Team), BSM (Stephen M. Brincat), DKS (Shawn Dvorak), Ioh (Hiroshi Itoh), BJA (Boardman James) and UJH (Joseph Ulowetz)

Table E3. Log of observations of the 2016 outburst in ASASSN-16hg.

Start*	End*	Mag [†]	Error [‡]	N^{\S}	Obs
57482.1006	57586.9298	14.450	0.026	126	HaC
57587.5914	57587.9316	14.573	0.033	124	HaC
57588.1796	57588.3012	15.827	0.042	65	KU1
57588.5700	57588.9314	14.673	0.042	147	HaC
57589.1455	57589.2971	15.919	0.055	86	KU1
57589.6285	57589.9299	14.838	0.038	106	HaC
57590.6264	57590.9293	15.367	0.083	101	HaC
57591.6232	57591.9304	14.866	0.081	118	HaC
57592.6389	57592.9300	14.733	0.050	112	HaC
57593.6371	57593.9296	14.839	0.056	113	HaC
57594.7362	57594.9297	14.967	0.041	65	HaC
57595.6319	57595.9309	15.075	0.047	95	HaC
57596.6855	57596.9303	15.185	0.031	121	HaC
57597.6264	57597.9300	15.324	0.037	137	HaC
57598.6237	57598.9295	16.262	0.144	138	HaC
57599.6210	57599.9281	18.176	0.392	126	HaC
57600.7491	57600.9295	18.736	0.441	89	HaC
57603.7192	57603.7192	18.403	–	1	HaC
57604.7336	57604.7336	15.578	–	1	HaC
57605.7310	57605.7310	16.637	–	1	HaC
57606.7283	57606.7283	18.031	–	1	HaC
57608.7227	57608.7227	15.622	–	1	HaC
57609.7199	57609.7209	16.703	0.012	2	HaC
57610.7175	57610.9250	18.200	0.250	189	HaC

*BJD – 2400000.0.

†Mean magnitude.

‡ 1σ of mean magnitude.

§Number of observations.

||Observer's code: see the annotation in Table E2.

Table E4. Times of superhump maxima in ASASSN-16dt.

E	Max [†]	Error	$O - C^{\ddagger}$	N^{\S}
0	57502.9004	0.0012	-0.0247	65
1	57502.9716	0.0008	-0.0181	64
21	57504.2745	0.0005	-0.0070	149
22	57504.3356	0.0007	-0.0104	148
23	57504.4028	0.0007	-0.0079	156
25	57504.5329	0.0007	-0.0069	50
31	57504.9243	0.0002	-0.0031	65
32	57504.9887	0.0002	-0.0033	63
33	57505.0547	0.0002	-0.0019	65
34	57505.1197	0.0002	-0.0015	65
36	57505.2494	0.0004	-0.0010	148
37	57505.3147	0.0004	-0.0002	200
38	57505.3793	0.0003	-0.0002	215
39	57505.4454	0.0003	0.0013	262
40	57505.5101	0.0004	0.0013	108
41	57505.5745	0.0004	0.0011	68
42	57505.6390	0.0003	0.0011	69
43	57505.7049	0.0003	0.0024	70
48	57506.0299	0.0003	0.0045	63
49	57506.0938	0.0006	0.0038	65
50	57506.1587	0.0004	0.0041	47
56	57506.5464	0.0006	0.0042	31
57	57506.6115	0.0005	0.0047	29
58	57506.6779	0.0009	0.0065	29
62	57506.9337	0.0003	0.0039	65
63	57506.9993	0.0003	0.0049	63
64	57507.0630	0.0003	0.0041	64
71	57507.5157	0.0008	0.0046	19
72	57507.5827	0.0005	0.0070	30
73	57507.6449	0.0005	0.0046	14
74	57507.7117	0.0009	0.0068	14
87	57508.5507	0.0005	0.0061	31
88	57508.6136	0.0006	0.0044	22
89	57508.6807	0.0007	0.0069	21
90	57508.7405	0.0010	0.0022	21
94	57509.0044	0.0010	0.0077	60
95	57509.0661	0.0007	0.0048	90
96	57509.1266	0.0007	0.0007	95
102	57509.5199	0.0015	0.0064	23
103	57509.5855	0.0007	0.0075	28
104	57509.6483	0.0012	0.0057	20
105	57509.7150	0.0010	0.0078	21
113	57510.2308	0.0003	0.0069	127
114	57510.2936	0.0003	0.0050	149
116	57510.4223	0.0003	0.0045	148
118	57510.5519	0.0005	0.0050	42
119	57510.6181	0.0009	0.0066	21
120	57510.6829	0.0008	0.0068	21
121	57510.7510	0.0016	0.0102	17
129	57511.2585	0.0005	0.0010	145
130	57511.3257	0.0005	0.0036	149

Table E4. Times of superhump maxima in ASASSN-16dt (continued).

E	Max [†]	Error	$O - C^{\ddagger}$	N^{\S}
131	57511.3881	0.0006	0.0015	128
134	57511.5819	0.0007	0.0015	37
135	57511.6469	0.0016	0.0019	21
136	57511.7104	0.0013	0.0008	21
141	57512.0316	0.0013	-0.0010	30
144	57512.2265	0.0009	0.0002	120
145	57512.2919	0.0004	0.0010	147
146	57512.3573	0.0004	0.0017	149
147	57512.4256	0.0006	0.0055	106
149	57512.5517	0.0006	0.0024	42
150	57512.6152	0.0022	0.0013	19
151	57512.6799	0.0010	0.0014	19
152	57512.7418	0.0020	-0.0013	15
154	57512.8690	0.0003	-0.0033	48
155	57512.9360	0.0004	-0.0009	65
156	57513.0018	0.0004	0.0003	62
157	57513.0665	0.0005	0.0004	65
158	57513.1325	0.0004	0.0019	103
163	57513.4509	0.0005	-0.0027	199
166	57513.6463	0.0006	-0.0011	55
167	57513.7092	0.0007	-0.0028	38
170	57513.9048	0.0004	-0.0010	65
171	57513.9709	0.0004	0.0005	63
172	57514.0354	0.0005	0.0005	65
173	57514.0967	0.0005	-0.0028	65
175	57514.2292	0.0040	0.0005	69
176	57514.2910	0.0008	-0.0023	123
177	57514.3561	0.0013	-0.0018	115
178	57514.4225	0.0008	0.0000	149
181	57514.6159	0.0010	-0.0004	176
182	57514.6785	0.0012	-0.0023	136
183	57514.7412	0.0012	-0.0043	116
185	57514.8640	0.0011	-0.0107	47
186	57514.9381	0.0006	-0.0011	65
187	57515.0012	0.0004	-0.0026	63
188	57515.0648	0.0006	-0.0036	65
189	57515.1308	0.0006	-0.0022	65
196	57515.5853	0.0025	0.0001	117
197	57515.6400	0.0012	-0.0098	97
198	57515.7086	0.0015	-0.0057	88
211	57516.5537	0.0020	-0.0003	53
212	57516.6127	0.0025	-0.0059	122
213	57516.6737	0.0011	-0.0095	124
214	57516.7433	0.0043	-0.0045	92
263	57519.9120	0.0008	-0.0008	64
264	57519.9789	0.0021	0.0015	44
293	57521.8583	0.0007	0.0077	44
294	57521.9259	0.0014	0.0107	65
295	57521.9903	0.0009	0.0105	64

*Cycle counts.

†BJD-2400000.0.

‡ $C = 2457502.925071 + 0.0653055 E$.

§Number of points used for determining the maximum.

Table E5. Times of superhump maxima in ASASSN-16hg.

E	Max [†]	Error	$O - C^{\ddagger}$	N^{\S}
0	57591.6600	0.0065	-0.0010	18
1	57591.7237	0.0037	0.0003	18
2	57591.7863	0.0013	0.0006	19
3	57591.8442	0.0015	-0.0038	21
4	57591.9102	0.0015	-0.0002	20
16	57592.6570	0.0012	-0.0015	16
17	57592.7208	0.0014	-0.0001	18
18	57592.7796	0.0016	-0.0037	19
19	57592.8439	0.0017	-0.0017	21
20	57592.9060	0.0016	-0.0020	21
32	57593.6548	0.0022	-0.0013	15
33	57593.7179	0.0011	-0.0006	18
34	57593.7767	0.0012	-0.0041	19
35	57593.8421	0.0017	-0.0011	20
36	57593.9059	0.0016	0.0004	20
50	57594.7769	0.0021	-0.0015	16
51	57594.8361	0.0018	-0.0046	17
52	57594.9042	0.0015	0.0011	17
64	57595.6516	0.0017	0.0003	14
65	57595.7146	0.0048	0.0010	15
66	57595.7729	0.0016	-0.0030	16
67	57595.8356	0.0015	-0.0027	16
68	57595.9068	0.0015	0.0061	15
81	57596.7117	0.0018	0.0006	15
82	57596.7738	0.0032	0.0003	27
83	57596.8389	0.0030	0.0030	28
84	57596.8956	0.0022	-0.0026	28
96	57597.6508	0.0027	0.0044	14
97	57597.7086	0.0029	-0.0001	15
98	57597.7678	0.0033	-0.0032	25
99	57597.8382	0.0059	0.0048	28
100	57597.8903	0.0047	-0.0055	28
114	57598.7596	0.0037	-0.0090	23

*Cycle counts.

†BJD-2400000.0.

‡ $C = 2457591.6610 + 0.0623475 E$.

§Number of points used for determining the maximum.